Radial localization of edge modes in Alcator C-Mod pedestals using optical diagnostics

C Theiler[1], J L Terry [2], E Edlund[3], I Cziegler[4], R M Churchill[3], J W Hughes[2], B. LaBombard[2] ,T. Golfinopoulos[2] and the Alcator C-Mod Team[1, 2, 3, 4]

[1)] *Ecole Polytechnique Federale de Lausanne (EPFL), Swiss Plasma Center (SPC), CH-1015 Lausanne, Switzerland*

[2)] *Plasma Science and Fusion Center (PSFC), Massachusetts Institute of Technology (MIT), Cambridge, MA 02139, USA*

[3)] *Princeton Plasma Physics Laboratory (PPPL), Princeton, New Jersey 08543, USA*

[4)] *York Plasma Institute, Department of Physics, University of York, Heslington, York, YO10 5DD, UK*

(Dated: 30 November 2016)

Dedicated experiments in ion cyclotron range heated Enhanced D-alpha (EDA) H-mode and I-mode plasmas have been performed on Alcator C-Mod to identify the location of edge fluctuations inside the pedestal and to determine their plasma frame phase velocity. For this purpose, measurements from gas puff imaging (GPI) and gas puff charge exchange recombination spectroscopy (GP-CXRS) have been collected using the same optical views. The data suggest that the EDA H-mode-specific quasi-coherent mode (QCM) is centered near the radial electric field (E_r) well minimum and propagates along the ion diamagnetic drift direction in the plasma frame. The weakly coherent mode (WCM) and the geodesic acoustic mode (GAM) observed in I-mode, on the other hand, are found to be located around the *outer* shear layer of the E_r well. This results in a weak plasma frame phase velocity mostly along the electron diamagnetic drift direction for the WCM. The findings in these EDA H-mode plasmas differ from probe measurements in ohmic EDA H-mode [B. LaBombard et al., Phys. Plasmas 21, 056108 (2014)], where the QCM was identified as an electron drift-wave located several mm outside the E_r well minimum in a region of positive E_r. To explore if instrumental effects of the optical diagnostics could be the cause of the difference, a synthetic diagnostic for GPI is introduced. This diagnostic reproduces amplitude ratios and relative radial shifts of the mode profiles determined from poloidally and toroidally oriented optics and, if instrumental effects related to GP-CXRS are also included, indicates that the measured location of the QCM and WCM relative to the E_r well reported here is only weakly affected by instrumental effects.

I. INTRODUCTION

The improved energy confinement achieved in high-confinement (H-mode) regimes might be a necessity for an economical fusion reactor. However, the steep profiles which form in the H-mode edge transport barrier, with pedestal-like profiles typically both for density and temperature, often lead to intermittent relaxations in the form of edge-localized modes (ELMs). The power fluxes to material surfaces caused by these ELMs constitute a serious issue for ITER and future reactors[1]. Therefore, besides developing ways to suppress or mitigate ELMs[2,3], a promising alternative is the development of high-confinement regimes without ELMs, such as QH-mode[4], EDA H-mode[5], and I-mode[6]. In the latter two examples, a continuous relaxation mechanism limits the edge gradients and keeps them below the peeling-ballooning boundary which determines the ELM onset[7,8]. It is believed that the enhanced particle transport and impurity flushing in these pedestals is provided by specific mode features observed in the fluctuation spectra, the quasi-coherent mode (QCM) in EDA H-mode and the weakly-coherent mode (WCM) in I-mode.

Unfortunately, the physical understanding of these fluctuations is hampered by the difficulty to experimentally determine important properties, such as their exact location in the edge barrier and their plasma frame phase velocity, i.e., their phase velocity in the frame moving with the local $E \times B$ drift. The difficulty arises because measurements from different diagnostics usually need to be combined to obtain a detailed picture. This results in uncertainties in the radial alignment of the different measured quantities, either simply because of uncertainties in the spatial calibration of the individual diagnostics, or due to uncertainties in mapping measurements along magnetic flux surfaces. Furthermore, the individual diagnostics can suffer from different instrumental effects. In devices with very narrow edge pedestals, such as in Alcator C-Mod[9], these alignment issues are especially challenging.

Recently, significant progress has been made in the identification of the EDA H-mode-specific QCM using the Mirror Langmuir Probe (MLP) on Alcator C-Mod[10]. A three stage, self-adaptive switch of the probe voltage on a time scale faster than the turbulence time scale provides the time resolved probe current-voltage characteristic and therefore the time histories of electron density, temperature, and plasma potential, all from a single probe tip. Radially scanning the probe across the scrape-off layer (SOL) and up to a few mm inside

the last closed flux surface (LCFS) therefore provides detailed measurements of time averaged and fluctuation profiles. These measurements found that the QCM is located in a region of positive radial electric field (E_r) around the LCFS and is propagating with the electron diamagnetic drift velocity in the plasma frame[10].
A drawback of scanning Langmuir probes (LPs) in general is the limited accessibility of the pedestal due to high heat fluxes. The experiments mentioned in the previous paragraph were therefore performed in modest power, ohmic EDA H-mode plasmas. One also needs to be careful about plasma perturbation by the probe and interpretation of the measurements, such as e.g. the effect of changes in the secondary electron emission coefficient, which enters in the evaluation of the plasma potential from measurements of the floating potential and the electron temperature.

In this paper, we report on experiments conducted on the Alcator C-Mod tokamak[11–13] to determine the radial location of quasi-coherent edge fluctuations in the pedestal using optical diagnostics. The experiments are conducted in ion cyclotron range heated plasmas. This assures good signal levels for the optical diagnostics and extends the MLP study of the QCM to higher power EDA H-modes. In addition, the use of optical diagnostics allows us to probe the WCM and the geodesic acoustic mode (GAM) in the I-mode pedestal, which is even more difficult to access with probes. The fluctuation measurements reported here are obtained with the gas puff imaging (GPI) diagnostic and time average profiles of impurity temperature, density, flows, and the $E \times B$ drift velocity are achieved with gas puff charge exchange recombination spectroscopy (GP-CXRS). The CXRS views of the pedestal were connected interchangeably to the CXRS and GPI detectors, respectively. This allowed us to obtain measurements of both pedestal profiles and edge fluctuations through the same optics, thus avoiding uncertainties associated with using different, toroidally separated optics.
This paper is organized as follows. In Sec. II, we present the experimental setup and the diagnostics. In Sec. III, we detail the approach to align GPI and GP-CXRS measurements, followed by the experimental results in III A and the consequences in terms of plasma frame phase velocities in III B. In Sec. IV, we explore the role of instrumental effects on the measurements. Sec. IV A introduces a synthetic diagnostic for GPI and results are discussed in Sec. IV B. Net relative shifts between mode profiles and E_r, including also instrumental effects related to GP-CXRS, are discussed in Sec. IV C. Finally, summary and conclusions are presented in Sec. V.

II. EXPERIMENTAL SETUP AND DIAGNOSTICS

The experiments reported here are performed in EDA H-mode and I-mode, two stationary, improved confinement regimes without ELMs routinely achieved on Alcator C-Mod. Enhanced D-alpha (EDA) H-mode[5] is a relatively high collisionality regime with pedestal collisionality $\nu^\star = \hat{\nu}_{ii} qR/(\epsilon^{1.5} v_{th,i}) \gtrsim 1$. It typically exhibits much higher D_α light intensity than (non-stationary) ELM-free operation, hence the name. Details on EDA H-mode access and comparisons to ELMy and ELM-free H-mode can be found in[7,9]. In EDA H-mode, global particle and impurity transport are strongly enhanced compared to ELM-free H-mode and regulated by continuous fluctuations rather than ELMs. This enhanced particle transport is ascribed to the QCM, an approximately field-aligned edge fluctuation with frequency and outer-midplane poloidal wave number of typically $f \approx 100$ kHz and $k_{pol} \approx 1.5$ cm^{-1}. The QCM was shown to indeed drive an outward radial particle transport at the low-field side (LFS)[10] and the effective pedestal particle diffusivity increases with the QCM amplitude[14]. Recent progress in the understanding of the QCM include the identification of the QCM as a LCFS spanning electron drift-wave with interchange and electromagnetic contributions[10] and the excitation of QCM-like fluctuations using a dedicated LFS antenna[15].
The EDA H-mode plasmas studied here are obtained in reversed field, upper single-null configuration, with the ion gradB drift towards the active X-point. Values of the line-averaged electron density, current, toroidal field, and additional heating power are $\bar{n}_e \approx 2.9 \times 10^{20}$m^{-3}, $I_p = 0.9$ MA, $B_T = 5.4$ T, and $P_{RF} = 1.5$ MW, respectively. The QCM frequency and mode number are $f = 86 \pm 6$ kHz and $k_{pol} = 1.9 \pm 0.8$ cm^{-1}, measured with GPI at the LFS midplane.
In contrast to EDA H-mode, I-mode[6,16,17] is a low collisionality regime, with typically $0.1 \leq \nu^\star \leq 1$. It is usually obtained with the ion gradB drift away from the active X-point. In I-mode, energy confinement is H-mode like, while particle confinement is similar to that in L-mode[6] and wall conditioning with recent boronization is not necessary for I-mode access. Characteristic of I-mode is also an edge pedestal in temperature but not in density. The typical absence of ELMs in these pedestals is consistent with peeling-ballooning stability calculations[7,8]. The threshold conditions for transitions from L- to I-mode and from I- to H-mode have been documented in[18] and recent multi-machine studies (ASDEX Upgrade, DIII-D, and Alcator C-Mod) indicate that the power window for I-mode access increases with toroidal field[19].
At the L-I transition, mid-frequency fluctuations ($f \sim 50 - 150$ kHz) are reduced and higher frequency, electromagnetic fluctuations appear[6,17]. These higher frequency fluctuations are referred to as the WCM. The WCM frequency and wave vector are typically $f \approx 100 - 300$ kHz and $k_{pol} \approx 1.5$ cm^{-1}. It is believed that the WCM plays a similar role as the QCM in EDA H-mode in regulating impurity and particle transport[20]. There are, however, clear differences when compared to the QCM. The WCM is significantly less coherent.

Also, measurements with an electron cyclotron emission radiometer show that temperature fluctuations associated with the WCM are an order of magnitude smaller than density fluctuations[21]. In comparison, QCM fluctuations in temperature are larger than in density[10]. A peculiarity of the WCM is also that it coexists and non-linearly interacts with coherent fluctuations in the 20 kHz range, which have been identified as a geodesic acoustic mode (GAM)[22]. Recent simulations with a six-field two-fluid model indicate that the I-mode pedestal is linearly unstable to drift Alfven wave instabilities and the resistive ballooning mode and the non-linear evolution reproduces a number of the properties of the WCM[23].
The I-mode plasmas discussed in the following have been obtained in reversed field, lower single null geometry, with the ion gradB drift away from the active X-point and with $\bar{n}_e \approx 1 \times 10^{20}\mathrm{m}^{-3}$, $I_p = 1$ MA, $B_T = 5.4$ T, and $P_{RF} = 3$ MW. WCM frequency and mode number are $f = 140 \pm 50$ kHz and $k_{pol} = 1.6 \pm 0.8$ cm^{-1}.

The main diagnostic techniques used in this work are gas puff imaging (GPI) and gas puff charge exchange recombination spectroscopy (GP-CXRS). GPI[24–27] images light emission from a localized gas puff using optical chords that are approximately parallel to the magnetic field in the region of the gas puff with 2MHz acquisition. Using a two-dimensional (2D) array of chords and given that plasma parameters vary little along the magnetic field across the toroidal extent of the gas puff, GPI essentially provides 2D measurements of edge turbulence. Usually, the collected light is filtered around the D_α, $\lambda = 656$ nm line for deuterium puffs and the HeI, $\lambda = 587.6$ nm line for helium puffs. In this work, helium puffs are used for GPI, as they have the advantage of very good signal to noise ratios due to negligible light emission from regions outside the puff. A recent description of the GPI system on C-Mod can be found in[28].
GP-CXRS[29,30] relies on charge exchange reactions of a localized source of neutrals with fully stripped impurities. The line radiation emitted after electrons transferred to the impurities relax to a lower energy state is collected with toroidal and poloidal optical chords. Spectroscopically analyzing this line emission then provides measurements of impurity temperature, flow, and radiance. From the latter, in combination with simultaneous measurements of radial profiles of the D_α emission and known atomic rate coefficients, the impurity density can be determined[29,30]. In contrast to traditional CXRS[31–33], where a high energy neutral beam is used as a neutral source to locally induce charge exchange reactions, the GP-CXRS technique uses a thermal gas puff instead. The density of neutrals generated this way decreases rapidly as a function of distance into the plasma. For the edge region of Alcator C-Mod, however, GP-CXRS gives light levels substantially larger than achieved with a diagnostic neutral beam[29]. From the quantities measured with the GP-CXRS diagnostic, the radial electric field is deduced using the radial impurity force balance

$$E_r = \frac{1}{n_z Z e}\frac{\mathrm{d}(n_z T_z)}{\mathrm{d}r} - V_{z,\theta}B_\phi + V_{z,\phi}B_\theta, \qquad (1)$$

where n_z is the impurity density, Z is the charge state of the impurities, T_z their temperature, $V_{z,\theta}$ and $V_{z,\phi}$ the poloidal and toroidal velocity, and B_θ and B_ϕ the poloidal and toroidal components of the magnetic field. The impurity species studied with GP-CXRS on C-Mod is fully stripped boron ($Z = 5$) using the BV ($n = 7 \rightarrow 6$) transition at $\lambda = 494.467$ nm. The integration time is typically 5 ms and does not allow resolving turbulent fluctuations.
The contribution of the individual terms on the right of Eq. (1) to the evaluation of E_r in EDA H-mode and I-mode have been presented in Ref.[34]. It is worth mentioning that the impurity diamagnetic term, the first term on the right of Eq. (1), contributes substantially to the evaluation of the E_r well, particularly in EDA H-mode. In H-mode, this term is dominated by the gradients in n_z, while in I-mode, gradients in n_z and T_z contribute approximately equally.

III. EXPERIMENTAL APPROACH TO ALIGN GPI AND CXRS EDGE MEASUREMENTS

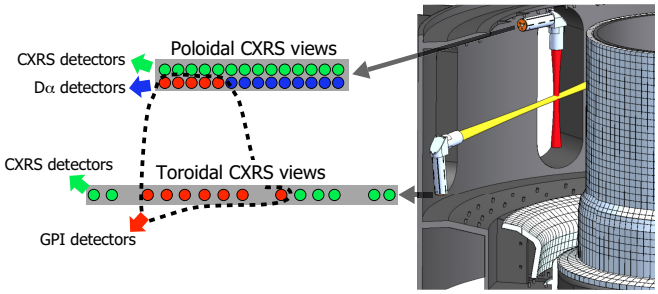

FIG. 1. Sketch of the edge CXRS optics, consisting of two radial rows of poloidal views and one row of toroidal views. The dashed curve at the left highlights views which, for some of the shots, have been connected to the GPI detectors to obtain fluctuation measurements.

The procedure to align GPI and CXRS measurements is illustrated in Fig. 1. The optics from the gas puff CXRS system consist of two radial rows of 14 poloidally oriented views and one row of 14 toroidally oriented views. The lines of sight together with the light-collecting periscopes are shown in a three-dimensional sketch of the interior of the C-Mod vacuum vessel in the right of Fig. 1. The individual views are schematically represented in the left of Fig. 1 by green, blue, and red circles. They have a spot size (diameter) of approximately 3 mm. Careful in-vessel calibrations have been performed to determine the radial location of the individual views. During an opening of C-Mod, poloidal and toroidal views have been

back-illuminated and the position of the optical path in front of the gas puff nozzle has been determined with an accuracy of ≈ 0.3mm. The two rows of poloidal views are essentially equivalent. In the plane of best focus, they are toroidally separated by 3 mm and are shifted radially with respect to each other by ≤ 0.2 mm.

In a series of at least two similar discharges, initially the system is operated in the standard CXRS setup. That is, the toroidal views and one of the poloidal rows of views are connected to the CXRS spectrometers, while the other poloidal set of views is connected to photodiodes in order to measure the D_α emission[29]. In this setup, the active charge exchange emission induced by a deuterium gas puff allows obtaining radial profiles of density, temperature, and poloidal and toroidal flows of fully stripped boron and, using Eq. (1), the radial electric field. The D_α emission measurements are needed to infer the gas puff neutral density, which in turn is needed for the evaluation of the boron density[30].
In a subsequent discharge, five of the poloidal D_α views and seven of the toroidal views are connected to the fast GPI detectors, which are capable of measuring the profiles of the fluctuations. These views are highlighted in Fig. 1 in red and circled by the dashed curve. They are selected to assure a good coverage of the mode region. A helium gas puff is used now, for the reasons discussed in Sec. II, and the radial mode profiles are determined from time domain Fourier analysis. Note that in this configuration, the other set of poloidal views is still connected to the CXRS detectors, such that radial profiles of impurity temperature and poloidal flow can still be obtained.
In summary, with a minimum of two discharges, this procedure allows us to get the full set of CXRS measurements, including the E_r profile, as well as the mode profile from GPI for both poloidal and toroidal optics. GPI and CXRS measurements are obtained using the same optics. For all discharges, profiles of impurity temperature and poloidal flow are available, allowing us to check for shot-to-shot changes of the plasma or profile shifts not accounted for in the equilibrium reconstruction.

A. Experimentally determined alignment

We now discuss the experimental results of the above procedure in EDA H-mode and I-mode. For both regimes, we have a discharge with a deuterium puff and several ones with a helium puff (two in EDA H-mode and five in I-mode). As mentioned above, the mode profiles were measured from He puffs.

In Figs. 2 and 3, we show power spectral densities (PSDs) of GPI signals at radial locations near the peak of the respective mode profiles. These PSDs are normalized by the square of the zero-frequency Fourier component. This is equivalent to plotting the PSD of $I_{GPI}/\langle I_{GPI}\rangle_t$, where I_{GPI} is the recorded GPI signal and the brackets indicate a time average. To evaluate the mode amplitude normalized in this way, we take the square root of these PSDs, subtract the background turbulence, and integrate over the mode feature.

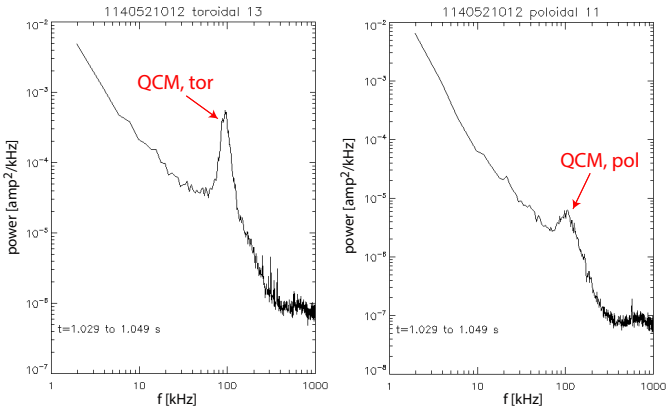

FIG. 2. GPI spectra in EDA H-mode near the peak of the QCM profile from toroidal (left) and poloidal (right) chords.

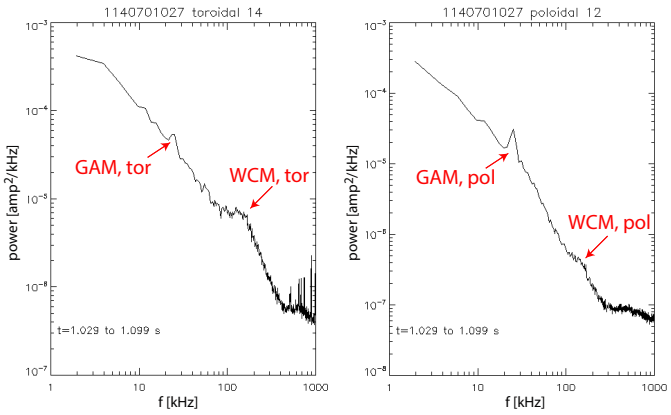

FIG. 3. GPI spectra in I-mode near the peak of the WCM/GAM profile from toroidal (left) and poloidal (right) chords.

We see that the characteristic features, the QCM in EDA H-mode and the WCM and the GAM in I-mode, are present in the spectra from both the toroidal and the poloidal views. It is also apparent from these plots and seen consistently throughout all our data that the QCM and WCM amplitudes are larger on the toroidal views as compared to the poloidal views. This can be explained by the fact that while the toroidal views are oriented approximately perpendicular to the wave-vector $\mathbf{k}$ of the mode, the poloidal optics are primarily along $\mathbf{k}$. As discussed in more detail in Sec. IV B, the latter can strongly reduce the mode amplitude, as long as the poloidal wave length of the mode is comparable or smaller than the width of the gas puff. In contrast to the QCM and the WCM, the GAM amplitude is stronger for the poloidal views. The reason for this is not understood and we merely note here that we expect a very different form of density fluctuations associated with the GAM, namely a $m = 1$ (long poloidal wavelength), standing wave[35].

Before discussing in more detail the mode profiles, we now turn to CXRS data. Figs. 4 (a) and (c) show profiles of impurity temperature and flow from the EDA H-mode where a deuterium puff is used. We use here the flux surface label $\rho = r/a_0$ as the radial coordinate, where r is the radial distance of a flux surface at the LFS midplane from the magnetic axis and a_0 is the value of r for the LCFS (for the plasmas discussed here, $a_0 \approx 21$ cm). EFIT[36] equilibrium reconstructions are used for these evaluations. We see from Fig. 4 (a) that the temperatures measured with the poloidal and the toroidal optics agree well except on the furthest out views, where values reported from the toroidal optics are somewhat higher. The poloidal impurity flow in Fig. 4 (c) shows the characteristic peak in the pedestal region and is in the electron diamagnetic drift direction. The toroidal impurity flow is co-current and varies radially only weakly.

Figs. 4 (b) and (d) show CXRS measurements from the poloidal system for both the discharge with the D_2 puff and one where a He puff is used. Data from the two shots agree well, both for temperature and flow and the uncertainty of their radial alignment is estimated to be $\Delta\rho \approx 0.002$. Further into the plasma, data from the helium puff is rather noisy. This is due to the fact that the helium puff propagates less far into the plasma, leading to lower light levels. This is generally observed on C-Mod[29] and is understood from gas puff simulations[37].

Finally, in Figs. 4 (e) and (f), we show profiles of the impurity temperature and the radial electric field, with a clear E_r well just inside the LCFS. Also shown in Fig. 4 (f) are the radial profiles of the QCM amplitude, measured with the toroidal and the poloidal views. Mode profiles from two different time intervals during the puff are plotted in arbitrary units. As the plasma is radially displaced during that time, a resolution better than the radial spacing of the optical chords is achieved in this way. The QCM amplitude-profile measured using the poloidal views is only about 15% of that from the toroidal views, so profiles are rescaled here for better visibility.

Fig. 4 (f) suggests that the QCM is located in the pedestal region and peaks around the E_r well minimum. As E_r well and mode profiles are obtained using the same optics but from two different discharges, the main uncertainty in their relative radial alignment (aside from possible instrumental effects explored in Sec. IV) is related to the radial alignment of the two discharges based on their temperature and poloidal flow profiles, Figs. 4 (b) and (d). The associated uncertainty of this procedure of $\Delta\rho \approx 0.002$, as mentioned above, is small, corresponding to about a tenth of the mode FWHM or the width of the E_r well.

The result in Fig. 4 (f) is somewhat inconsistent given that there is a radial shift between the mode profiles obtained from poloidal and toroidal optics of $\Delta\rho \approx 0.006$ or $\Delta r \approx 1.3$ mm. Furthermore, the mode localisation relative to the E_r profile differs from results obtained with the MLP in an ohmic EDA H-mode, which showed that the QCM is located *outside* of the E_r well minimum, in the region of positive radial electric field[10]. This point will be further investigated in Sec. IV.

It should be noted that there is a rather important uncertainty in the position of the LCFS determined from the EFIT equilibrium reconstruction at the outboard midplane[10], as indicated by the shaded region in Fig. 4 (e-f). This uncertainty does, however, not enter in the relative alignment of E_r and mode profiles.

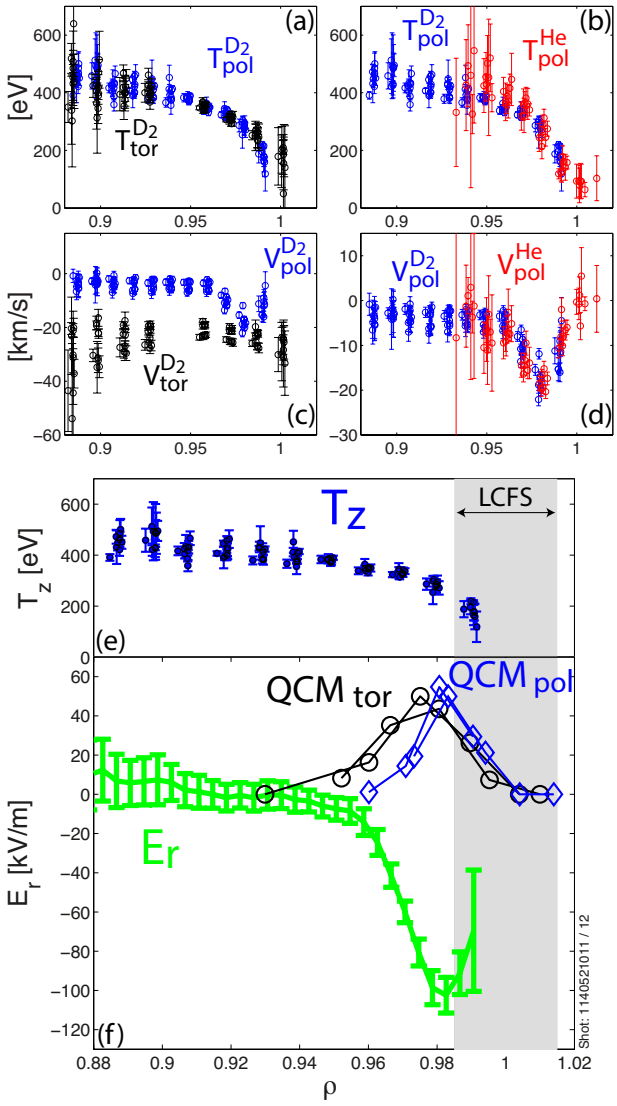

FIG. 4. Data from an EDA H-mode plasma. (a) and (c): impurity (B^{5+}) temperature and flow measured with toroidal and poloidal optics during a deuterium puff. (b) and (d): comparison of impurity temperature and flow measured with poloidal optics during a discharge with a deuterium and a helium puff, respectively. Subplots (e) and (f) show the results of combining GPI and CXRS measurements, with temperature and E_r profiles from CXRS and the QCM amplitude profiles from toroidal and poloidal optics using GPI. Mode profiles are shown in arbitrary units and rescaled, see main text. The shaded region indicates the uncertainty range of the LCFS.

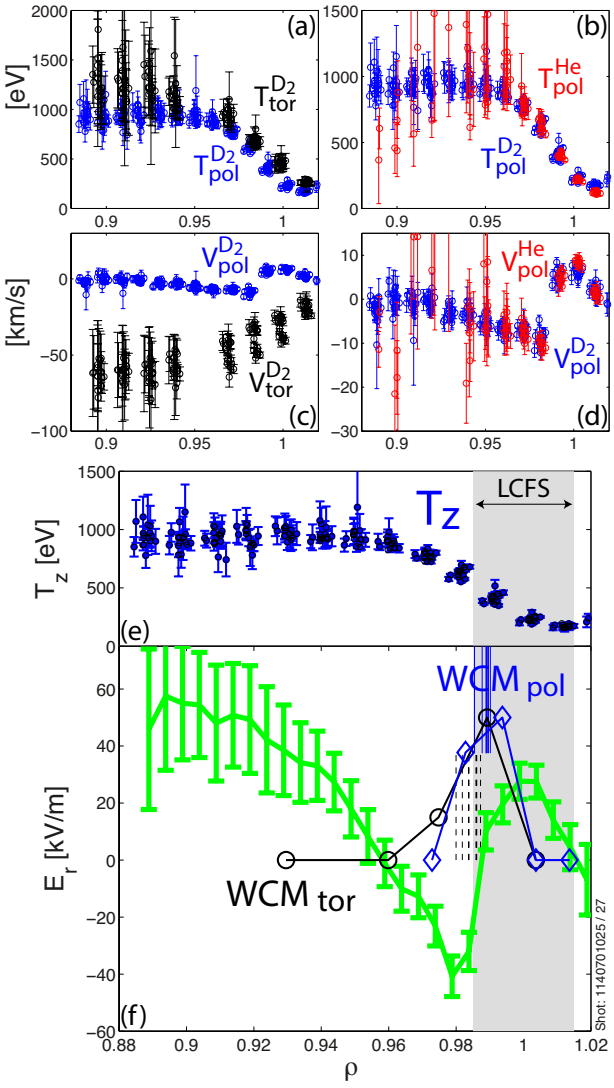

FIG. 5. The equivalent to Fig. 4 for I-mode. Vertical lines in (f) show the center of mass position of the WCM amplitude profiles measured with poloidal (solid) and toroidal (dashed) optics for different shots and time intervals.

We next discuss the experimental results in I-mode. The equivalent to Fig. 4 for I-mode is shown in Fig. 5. More clearly than in H-mode, Fig. 5 (a) reveals temperatures measured with the toroidal optics which exceed values from the poloidal system in the pedestal. Good agreement between the two temperature profiles would result if e.g. the T_{tor} profile was shifted in by ≈ 1.3 mm. However, this is substantially more than allowed based on the uncertainty in the spatial calibration of the optics. The poloidal flow in Fig. 5 (c) shows the typically observed strong shear near the LCFS, while the toroidal flow is again co-current. As in the case of H-mode, good agreement is found between poloidal CXRS data for the discharge with the deuterium puff and the helium puff, Fig. 5 (b) and (d). The E_r well, plotted in Fig. 5 (f), has an asymmetric structure characteristic for I-mode, with a stronger shear layer at the outer edge of the well[34]. Pro-

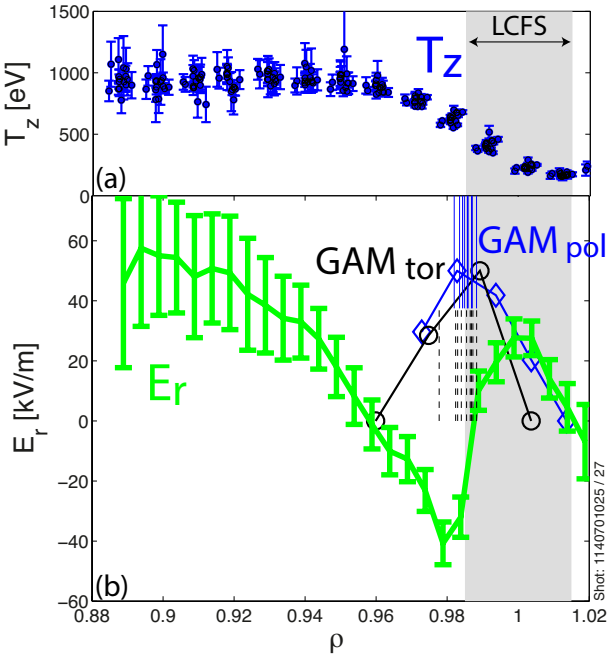

FIG. 6. The equivalent to Fig. 5 (e) and (f) for the GAM.

files of the WCM amplitude measured with toroidal and poloidal optics have been evaluated for five I-mode discharges and for different time intervals within these shots. In Fig. 5 (f), the center of mass locations for each of these WCM profiles are indicated by vertical lines, solid for poloidal, dashed for toroidal measurements. These lines represent, in a statistical manner, the uncertainty in the alignment of E_r and mode profiles due to uncertainties in the radial alignment of the deuterium and helium puff discharges as well as uncertainties in the WCM amplitude profile evaluation. The deduced mode radial locations are characterised by a spread with a standard deviation of $\Delta\rho \approx 0.0025$ ($\mathrm{WCM_{tor}}$) and $\Delta\rho \approx 0.0018$ ($\mathrm{WCM_{pol}}$). As in the EDA H-mode case, these uncertainties are much smaller than the width of the mode or the E_r well.

Example profiles of the WCM from toroidal and poloidal measurements are also plotted in Fig. 5 (f). As for the QCM, these WCM profiles are shown in arbitrary units and have been rescaled for better visibility. The actual amplitude ratio of the mode profiles measured with poloidal and toroidal optics varies for different shots between 0.09 and 0.44. The mode profiles measured with toroidal and poloidal optics are again shifted radially with respect to each other. However, this shift is weaker than in H-mode. On average, it is $\Delta\rho \approx 0.004$ or $\Delta r \approx 0.9$ mm. These measurements consistently place the WCM into the outer shear layer region of the E_r well. Fig. 6 shows the equivalent to Fig. 5 (e-f) for the GAM profiles. These mode profiles are again normalized. As mentioned above, the peak amplitude of the GAM on the poloidal optics exceeds that on the toroidal optics by a factor varying between 1.4 and 2.3 for the different shots.

The radial shift between poloidal and toroidal mode profiles is essentially absent here.

Consistent with Ref[22], we find that the locations of the WCM and the GAM closely align, but the measurements presented here show that their profile is located further out with respect to the E_r well than assumed in Ref[22]. It is worth mentioning here that in ASDEX-Upgrade I-mode plasmas, recent measurements based on reflectometry have localised the WCM in the E_r well minimum[38].

B. Consequences for plasma frame phase velocities

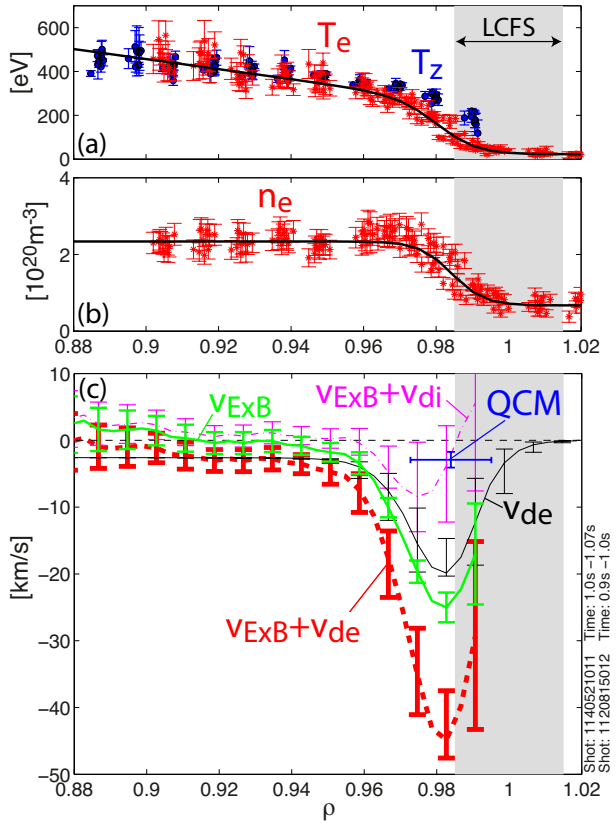

FIG. 7. (a-b): Thomson scattering profiles of n_e and T_e from an EDA H-mode similar to the one studied here with CXRS and GPI. In (a), the boron temperature profile is also shown. (c): Experimentally determined radial location and laboratory frame poloidal phase velocity of the QCM, together with possible contributions to its phase velocity. The shaded region indicates the uncertainty of the LCFS position.

We now discuss what the above measurements imply for the plasma frame phase velocity of the QCM and the WCM. In Fig. 7 (c), we plot different velocities of interest for the EDA H-mode case. The green curve represents the poloidal phase velocity we would observe if the mode was merely convected by the ExB flow. It is composed of two contributions. The main contribution comes from the poloidal projection of the ExB drift, $\frac{E_r}{B} \cdot \frac{B_\phi}{B}$. The other contribution comes from the toroidal projection of the ExB flow, which gives an apparent poloidal propagation due to the barber pole effect. This term is given by $\frac{E_r}{B} \cdot \frac{B_\theta^2}{BB_\phi}$, such that the sum of the two terms becomes $\frac{E_r}{B_\phi}$. Ref[10] found that the mode propagates approximately with the electron diamagnetic drift velocity in the frame moving with the ExB flow. The thin, black curve in Fig. 7 (c) is the contribution of the electron diamagnetic drift to the poloidal phase velocity for this case. Similarly to the ExB drift, it consists of a contribution from both poloidal and toroidal projection of the electron diamagnetic drift and is given by $\frac{1}{en_eB_\phi} \cdot \frac{\partial n_e T_e}{\partial r}$. This expression is evaluated from the profiles of n_e and T_e shown in Fig. 7 (a-b), which are obtained with the Thomson Scattering (TS) diagnostic[39]. As TS data was not available for the EDA H-modes studies here, data from a similar discharge is used instead. For the relative alignment of TS and CXRS data, we have assumed that the electron temperature pedestal is shifted in with respect to the boron temperature profile, also shown in Fig. 7 (a), by $\Delta\rho = 0.01$, corresponding to $\Delta r \approx 2$ mm. This shift is motivated by recent experimental and numerical results[34,40].

These flow profiles can now be compared with the experimentally-determined radial location and phase velocity of the QCM, indicated in Fig. 7 (c) with a blue cross hair. The radial QCM location is the one obtained from the poloidal optics in Sec. III A and the radial width of the cross hair represents the measured width of the mode profile. The phase velocity of the QCM is obtained from its wavenumber-frequency spectrum determined from the standard, two-dimensional GPI diagnostic[28], which is toroidally separated from the CXRS views and was operated simultaneously in these discharges. We can see that even though the QCM propagates in the electron diamagnetic drift direction in the laboratory frame, Fig. 7 (c) reveals a propagation in the ion diamagnetic drift direction in the plasma frame after accounting for the ExB convection. Determining the ion diamagnetic drift contribution, $v_{di} = \frac{-1}{en_iB_\phi} \cdot \frac{\partial n_i T_i}{\partial r}$, assuming $T_i = T_z$ and $n_i = n_e$, we actually find good agreement here between the QCM phase velocity and the sum of the ExB and the ion diamagnetic drift as also shown in Fig. 7 (c).

To obtain instead a plasma frame phase velocity similar to the electron diamagnetic drift, as observed with the MLP in ohmic EDA H-mode[10], the QCM in Fig. 7 (c) would need to be shifted out with respect to the E_r well by about $\Delta\rho \approx 0.015$, corresponding to $\Delta r \approx 3$ mm. The possibility that instrumental effects in the present measurements could introduce such a shift is investigated in Sec. IV.

In Fig. 8, we show the equivalent to Fig. 7 for I-mode and the WCM. Again, TS data from an I-mode discharge similar to the one studied here with CXRS and GPI is used. Motivated by the substantial poloidal asymmetries

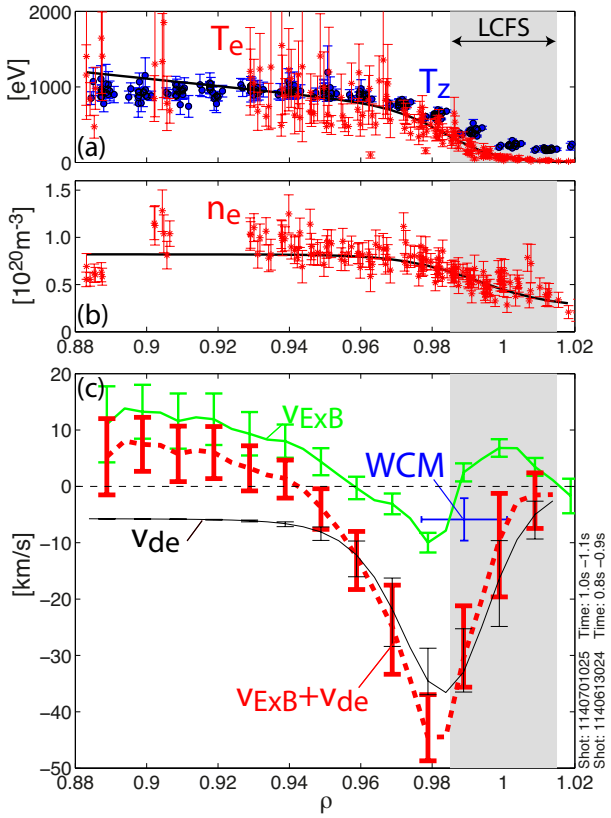

FIG. 8. The equivalent to Fig. 7 for I-mode.

in boron temperature in the I-mode pedestal[34], similarly to EDA H-mode, these TS profiles have been shifted inwards by $\Delta\rho = 0.01$ relative to T_z, as shown in Fig. 8 (a). It is apparent from Fig. 8 (c) that, as in the case of the QCM, the WCM propagates in the electron diamagnetic drift direction in the laboratory frame. Fig. 8 (c) indicates that this is also the case in the plasma frame across most of the experimentally determined mode profile. This plasma frame phase velocity is, however, substantially lower than the electron diamagnetic flow.

IV. INSIGHTS FROM A SIMPLIFIED SYNTHETIC DIAGNOSTIC

In the previous Sections, we have seen that, particularly in H-mode, there is a shift between the mode profiles measured with poloidal and toroidal optics. Furthermore, the QCM localization and plasma frame phase velocity differ qualitatively from the one determined previously with probe measurements in low power EDA H-mode[10]. In the following, we explore the possibility that instrumental effects of the optical diagnostics could be the cause of these discrepancies. For this purpose, we introduce and explore a simplified synthetic diagnostic for GPI light collection. We also discuss possible instrumental effect in the GP-CXRS measurements.

A. Description of the synthetic diagnostic

We assume that the emissivity of the HeI 587.6 nm line recorded with the GPI detectors is proportional to the local helium neutral density $n_{He}(\mathbf{x})$ and the electron density $n_e(\mathbf{x}, t)$. The latter is a simplification of the more realistic dependence on $n_e(\mathbf{x}, t)^\alpha \cdot T_e(\mathbf{x}, t)^\beta$ (Ref[41]). We further assume that in the vicinity of the gas puff, the optical chords are cylindrical and light is collected over the same solid angle for each volume element of the chord. For a given GPI view, the recorded signal, labelled I_{GPI}, is then given by:

$$I_{GPI} \propto \int_{V_{chord}} n_{He}(\mathbf{x}) n_e(\mathbf{x}, t) \mathrm{d}V. \qquad (2)$$

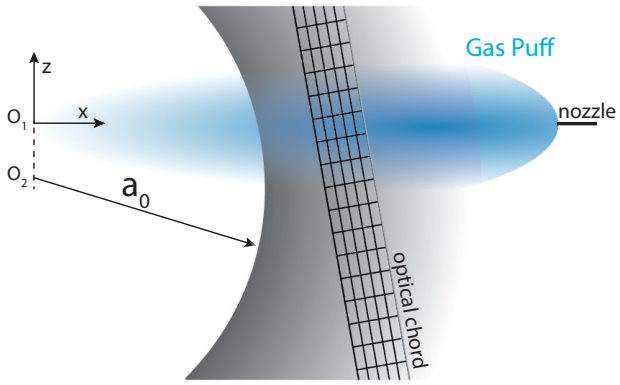

FIG. 9. Sketch of the synthetic GPI diagnostic in the poloidal plane, showing the gas puff, an optical chord, and the choice of the coordinate system.

We first discuss the poloidal optics and consider the geometry sketched in Fig. 9. In the poloidal plane and close to the gas puff, flux surfaces are well approximated by concentric circles. The circle with radius a_0 and origin O_2 which best approximates the LCFS in the vicinity of the gas puff is determined from outputs of the equilibrium reconstruction. Depending on the discharge, the origin O_2 can be shifted up or down with respect to the nominal $z = 0$ position of C-Mod (typically by $\leq$ 1cm). We define our coordinate system with its origin O_1 coinciding with the nominal $z = 0$ position and having the same radial position as O_2, as shown in Fig. 9. In these coordinates, the gas puff nozzle is located at $z = 0$ and we assume the following form for the neutral density $n_{He}(\mathbf{x})$ of the gas puff

$$n_{He}(\mathbf{x}) \propto \exp\left(\frac{x - a_0}{L_{He}}\right) \cdot \exp\left(-\frac{z^2}{W_{He}^2}\right). \qquad (3)$$

We will assume that the width W_{He} and the decay length L_{He} of the gas puff are independent of x, which is a simplification compared to the gas puff shapes determined for deuterium puffs using OSM-EIRENE simulations[29]. For the electron density $n_e(\mathbf{x}, t)$ appearing in Eq. (2),

we assume that it is composed of a poloidally symmetric, time-independent component and a poloidally propagating mode, whose amplitude is poloidally symmetric:

$$n_e(\mathbf{x},t) = \bar{n}_e(r) + \tilde{n}_e(r)\cdot\cos(k_{pol}r\theta + \frac{\mathrm{d}\varphi}{\mathrm{d}r}r - \omega t). \quad (4)$$

Here, the polar coordinates r and θ are defined with respect to O_2 in Fig. 9. The term $\frac{\mathrm{d}\varphi}{\mathrm{d}r}r$ in Eq. (4) allows for a radially sheared mode structure and $\bar{n}_e(r)$ and $\tilde{n}_e(r)$ are assumed to have the following shape

$$\bar{n}_e(r) = n_A\cdot\mathrm{mtanh}\left(\alpha_n, \frac{r_0 - r}{d}\right) + n_B \quad (5)$$

$$\tilde{n}_e(r) = n_{mode}\cdot\exp\left(-\frac{(r-r_{mode})^2}{W_{mode}^2}\right), \quad (6)$$

where mtanh is the modified hyperbolic-tangent function[42] defined as

$$\mathrm{mtanh}\,(\alpha_n, x) = \frac{(1+\alpha_n\cdot x)e^x - e^{-x}}{e^x + e^{-x}}. \quad (7)$$

Example profiles of $\bar{n}_e$ and $\tilde{n}_e$ along $z = 0$ are shown in Fig. 10 (a).

The integration over the volume of a cylindrical chord is performed by dividing it into small cells as shown in Fig. 9. For these poloidal views, variations in the toroidal direction, over the narrow width of the chord ($\approx$ 3mm), are neglected and each cell in Fig. 9 is simply weighted according to its (three-dimensional) volume. The finite tilt of the chords with respect to the vertical direction ($\approx 3.4°$) is taken into account and the radial spacing between chords is set to 0.2 mm to assure high radial resolution.

If we now define the quantities $\bar{I}_{GPI}$ and $\tilde{I}_{GPI}$ as follows

$$\bar{I}_{GPI} = \int_{V_{chord}} n_{He}(\mathbf{x})\bar{n}_e(r)\mathrm{d}V \quad (8)$$

$$\tilde{I}_{GPI} = \int_{V_{chord}} n_{He}(\mathbf{x})\tilde{n}_e(r)\cdot e^{i(k_{pol}r\theta + \frac{\mathrm{d}\varphi}{\mathrm{d}r}r)}\mathrm{d}V, \quad (9)$$

the mode amplitude, using the same normalization as discussed in Sec. III A, is given by

$$A = \frac{|\tilde{I}_{GPI}|}{\bar{I}_{GPI}}. \quad (10)$$

The synthetic diagnostic for the toroidal optics is modeled analogously. We take into account the curvature of the magnetic field lines as well as the angle of the chords with respect to the flux surface tangent at the center of the gas puff ($\approx 6°$). Motivated by Ref[29], we assume that the gas puff is cylindrically symmetric, such that Eq. (3) remains valid if we replace z by the distance from the symmetry axis of the puff. For the integration over the chord volume, we neglect the vertical variation of quantities over the narrow width of the chords ($\approx$ 3mm). In principle, we should take into account the tilt of the chords relative to a horizontal plane ($\approx 7°$) and the magnetic field line pitch ($\approx 10 - 12°$ for the plasmas considered here). However, we have verified that taking those effects into account and assuming $k_\parallel = 0$ gives results very similar to simply assuming a toroidally symmetric mode structure and chords lying in a horizontal plane.

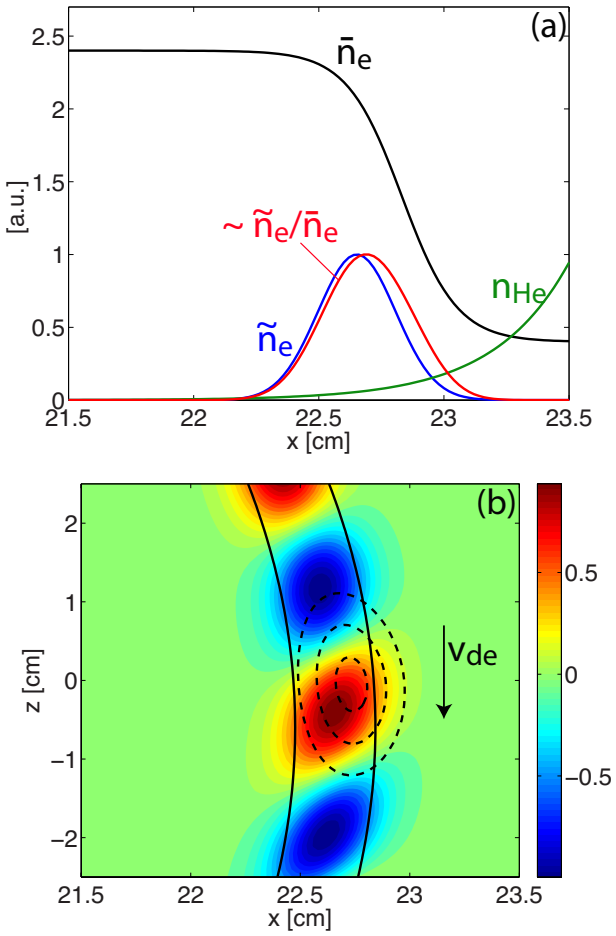

FIG. 10. Input profiles for the synthetic diagnostic for the EDA H-mode discharge. (a): radial profiles along the x-axis in Fig. 9. (b): Contour plot in the x-z plane of $\tilde{n}_e(r)\cdot\cos(k_{pol}r\theta + \frac{\mathrm{d}\varphi}{\mathrm{d}r}r)$ together with contours of $n_{He}(\mathbf{x})\tilde{n}_e(r)$ (dashed). The direction of the electron diamagnetic drift for this reversed field EDA H-mode is also indicated.

B. Results from the synthetic diagnostic

In Fig. 10, we show example profiles used in the synthetic diagnostic for the EDA H-mode discharge. Fig. 10 (a) shows profiles of $\bar{n}_e$, $\tilde{n}_e$, and n_{He} at $z = 0$. The $\tilde{n}_e$ profile has a width, W_{mode}, normal to the flux surfaces of 2.2 mm as determined from a fit to the poloidal measurement of the QCM profile in Fig. 4 (f). The profile of $\bar{n}_e$ is obtained from fitting Eq. (5) to electron density measurements from Thomson Scattering (again obtained

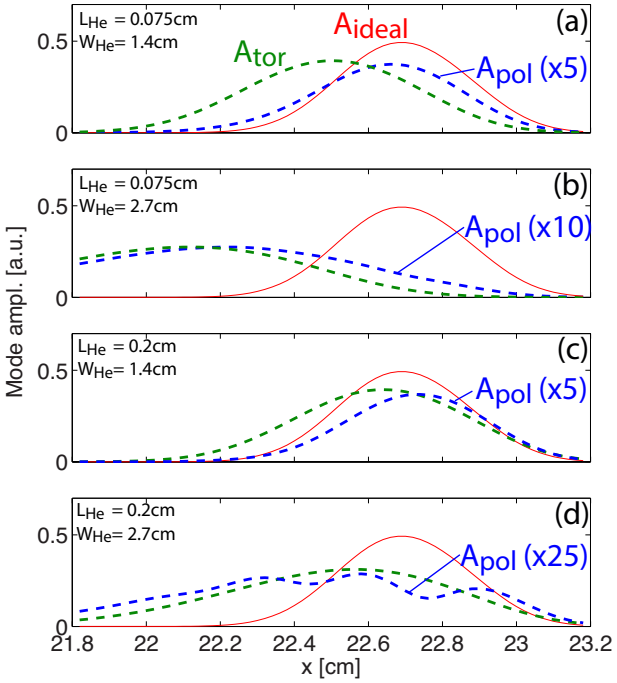

FIG. 11. Mode profiles evaluated with the synthetic diagnostic in EDA H-mode for the different values of L_{He} and W_{He} indicated in the plots. The mode profiles from the poloidal optics are rescaled as indicated.

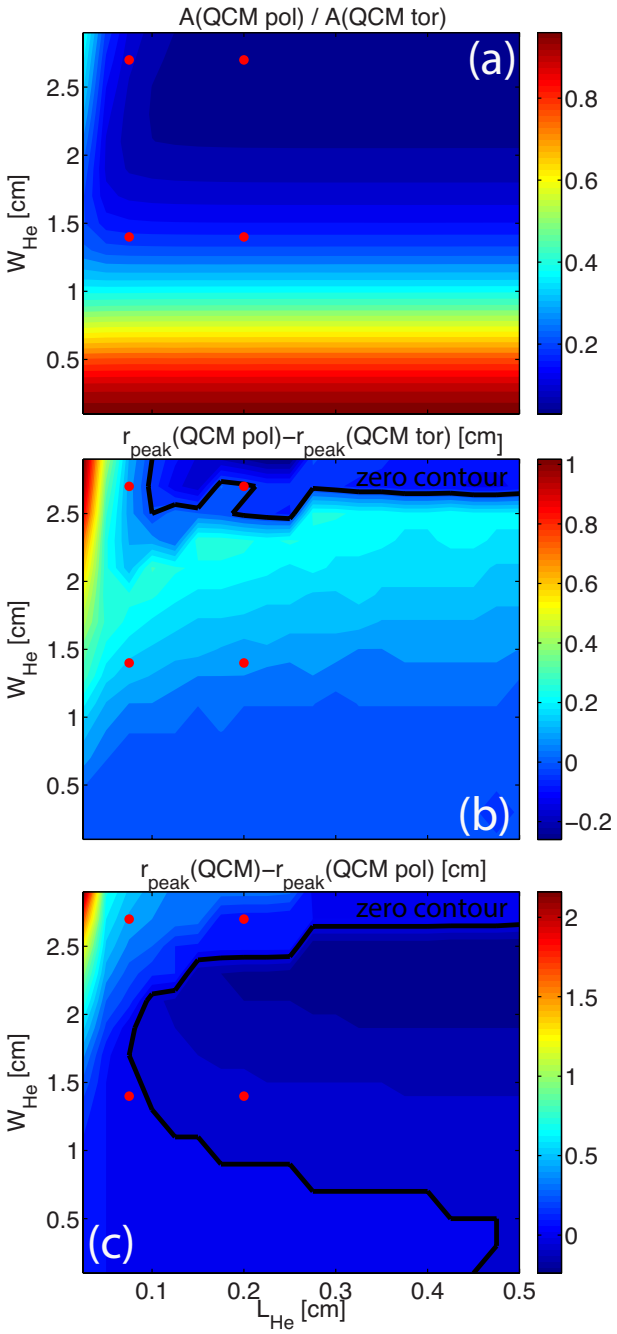

FIG. 12. Outputs of the synthetic diagnostic in EDA H-mode for different values of L_{He} and W_{He}. (a) shows the amplitude ratio of the mode profiles from poloidal and toroidal optics. (b) shows the radial distance between the peak of these profiles. (c) shows the radial distance between the peak of the actual mode profile and the poloidal one.

from a similar discharge, as the Thomson Scattering diagnostic was not available for these experiments). The radial alignment with respect to the mode profile is determined here by the requirement that impurity temperature T_z from GP-CXRS and electron temperature T_e from TS overlay (the effect of a finite relative shift will also be discussed). Also shown in Fig. 10 (a) is $\tilde{n}_e/\bar{n}_e$, which is the mode amplitude as measured with an ideal diagnostic (very narrow puff and optical chords) according to the definition in Eq. (10). Fig. 10 (b) shows a contour plot of $\tilde{n}_e(r) \cdot \cos(k_{pol} r\theta + \frac{\mathrm{d}\varphi}{\mathrm{d}r} r)$ in the $x - z$ plane, illustrating the assumed mode structure. The value of $\frac{\mathrm{d}\varphi}{\mathrm{d}r} \approx -2.5$ rad/cm has been determined from measurements of the simultaneously operated and toroidally displaced standard, two-dimensional GPI diagnostic. Solid contour lines in Fig. 10 (b) indicate the location where $\tilde{n}_e(r)$ has dropped to half its peak value. Dotted contours represent the quantity $n_{He}(\mathbf{x})\tilde{n}_e(r)$ appearing in the definition of $\tilde{I}_{GPI}$, Eq. (9). The curvature radius of the LCFS at the midplane is ≈ 23 cm here and its center is ≈ 0.6 mm below $z = 0$.

In Fig. 11, we show outputs of the synthetic diagnostic for four different gas puff shapes, parameterized by the width W_{He} and the radial decay length L_{He}. Shown are profiles of the mode amplitudes for the poloidal and the toroidal optics, as well as the actual mode profile, which is what an ideal diagnostic (negligible width of the optical chords and the gas puff) would measure. Fig. 11 (a) and (b) show the changes when W_{He} is increased from 1.4 cm to 2.7 cm at constant $L_{He} = 0.075$ cm. Fig. 11 (c) and (d) show the same for a less quickly decaying gas puff with $L_{He} = 0.2$ cm. We can see that, as in the experiment, the mode amplitude from the poloidal optics is weaker than that from the toroidal optics, and

drops with increasing W_{He}. This amplitude reduction is caused by phase canceling in the exponential in Eq. (9) when the puff width is comparable or larger than the poloidal wavelength of the mode.
The outputs of the synthetic diagnostic in Fig. 11 (a)-(c) are roughly consistent with the experimentally measured shift between poloidal and toroidal mode profiles of ≈ 1.3 mm and their amplitude ratio of ≈ 0.15. For the cases in Fig. 11 (a) and (c), the poloidal mode profile is centered very close to the actual mode profile, with a radial shift less than 1 mm. For the case in Fig. 11 (b), the mode profile simulated for the poloidal views is further in with respect to the actual mode profile by 4.6 mm. In this case, however, the radial width of the mode profile simulated for the poloidal views (≈ 6 mm) is much larger than the actually measured value (≈ 2.2 mm).

Results from more systematic scans in L_{He} and W_{He} with 0.025 cm $\leq L_{He} \leq$ 0.5 cm and 0.1 cm $\leq W_{He} \leq 2.9$ cm are shown in Fig. 12. The examples from Fig. 11 are indicated by red dots in these plots. Subplot (a) shows the amplitude ratio of the mode profiles obtained for poloidal and toroidal optics as a function of L_{He} and W_{He}. As expected, this reveals that the amplitude ratio depends strongly on W_{He}. It also depends on L_{He} for $L_{He} \lesssim 0.1$ cm and $W_{He} \gtrsim 1.5$ cm. This dependence on L_{He} is related to the tilt of the optical views and disappears when poloidal and toroidal optics are assumed to be perfectly tangential to the flux surfaces at the puff location. Fig. 12 (b) shows the radial shift between the maxima of the poloidal and toroidal mode profiles. This reveals that this shift is mostly positive, i.e. the poloidal mode profile is located further out than the toroidal one, except for $W_{He} \gtrsim 2.5$ cm. These relative shifts are approximately 2 mm for $W_{He} \approx 2$ cm and become negligible as W_{He} goes to zero. Finally, Fig. 12 (c) shows the radial shift between the maxima of the actual QCM profile and the one obtained from the poloidal optics. These shifts can be positive or negative, i.e., the QCM profile obtained from poloidal optics can appear shifted in or out. In particular, positive (inward) shifts of a few mm are observed for sufficiently small L_{He} and $W_{He} \gtrsim 1.5$ cm.

In Fig. 13 (a), we identify the region in the $L_{He} - W_{He}$ plane for which the synthetic diagnostic reproduces the experimentally measured amplitude ratio of ≈ 0.15 and radial shift of $\approx$ 1.3 mm of the QCM profiles from poloidal and toroidal optics. The black curves show the contour lines for a mode amplitude ratio of 0.1 and 0.2. The red area highlights the region where the shift between poloidal and toroidal profiles lies in the range between 1 mm and 1.6mm. This reveals that these two conditions are met in the synthetic diagnostic for $L_{He} \geq 0.075$ cm, $W_{He} \approx 1.5$ cm or $L_{He} \approx 0.075$ cm, $W_{He} \geq 2.7$. We note that from modeled deuterium gas puffs for C-Mod, summarised in Figure 2 of[29], we find that puff widths of 1-3 cm and decay length of 0.3 cm or even shorter are possible. From this, even steeper profiles for the more quickly decaying helium gas puffs with $L_{He} \approx 1$ mm seem not unrealistic. In the first region, $L_{He} \geq 0.075$ cm, $W_{He} \approx 1.5$ cm, we find that the simulated QCM profiles from the poloidal optics are shifted out with respect to the actual mode profiles by modest values between -0.2 and 1.2 mm. This would imply that the actual QCM profile in Fig. 4 (f) peaks between the toroidal and the poloidal mode profile. In the second region, $L_{He} \approx 0.075$ cm, $W_{He} \geq 2.7$, on the contrary, the poloidal mode profile appears shifted inwards by as much as 5 mm. However, as already mentioned in the discussion of Fig. 11 (b), these cases are inconsistent with the experiment in that the width of the mode, evaluated as W_{mode} =HWHM/$\sqrt{\log(2)}$, is with ≈ 6 mm much larger than the measured value of ≈ 2.2 mm.
We next explore if the experimental mode width can be reproduced for the small L_{He}, large W_{He} region if an input value of W_{mode} smaller than 2.2 mm is used. In Fig. 13 (b), the synthetic diagnostic result for $W_{mode} = 1.6$mm is shown. We see that the black contours of constant mode amplitude ratio have shifted to the right compared to Fig. 13 (a). For even smaller input values for W_{mode}, they move past the red region of realistic shifts between mode profiles. In Fig. 13 (b), the experimental mode ratio and shift are reproduced for $L_{He} \approx 0.075$cm and 1.9 cm $\leq W_{He} \leq 2.7$ cm. For these cases, the poloidal mode profile appears shifted in by 1.8 mm - 4.1 mm, while the obtained mode width is with 3.6 mm - 4.8 mm still substantially larger than in the experiment. For $L_{He} \geq 0.075$cm and $W_{He} \approx 1.5$ cm, realistic mode widths are obtained. For these cases, the poloidal mode position differs from the actual one by $\lesssim 1$ mm.
Besides the gas puff shape and the actual QCM width, another uncertainty entering the synthetic diagnostic is the radial position of the mode profile $\tilde{n}_e$ with respect to $\bar{n}_e$. First, the input for the radial mode location was deduced from the measured poloidal mode profile, which could be affected by instrumental effects. Second, the radial alignment of $\tilde{n}_e$ and $\bar{n}_e$ in the synthetic diagnostic was determined from experimental data by the assumption that impurity temperature and electron temperature overlay in the pedestal region. As already pointed out in Sec. III B, there is, however, experimental and numerical evidence that ion and electron temperatures can substantially differ in the steep gradient pedestals on C-Mod[34,40]. Therefore, in Fig. 13 (c) and (d), we investigate the sensitivity of the synthetic diagnostic on the shift between $\tilde{n}_e$ and $\bar{n}_e$. We find that by shifting the position of $\bar{n}_e$ in or out with respect to $\tilde{n}_e$ by 2 mm does not significantly change the results.
In summary, the synthetic diagnostic reproduces the experimentally observed mode ratios and shifts for gas puffs with $L_{He} \geq 0.075$ cm and $W_{He} \approx 1.5$ cm. In this case, the mode position determined from poloidal

optics is very close to the actual mode location. Large shifts are obtained for $L_{He} \approx 0.075$ cm, $W_{He} \geq 2$ cm. In these cases, however, the simulated mode width is substantially larger than in the experiment. It is worth mentioning that our synthetic diagnostic shows that toroidal optics would give a good mode localization for all of the explored values of L_{He} and W_{He} if the views were perfectly tangential to the flux surfaces near the gas puff. There would be a slight inward shift of ≈ 1 mm for $L_{He} = 0.025$ cm which already drops below ≈ 0.5 mm for $L_{He} = 0.1$.

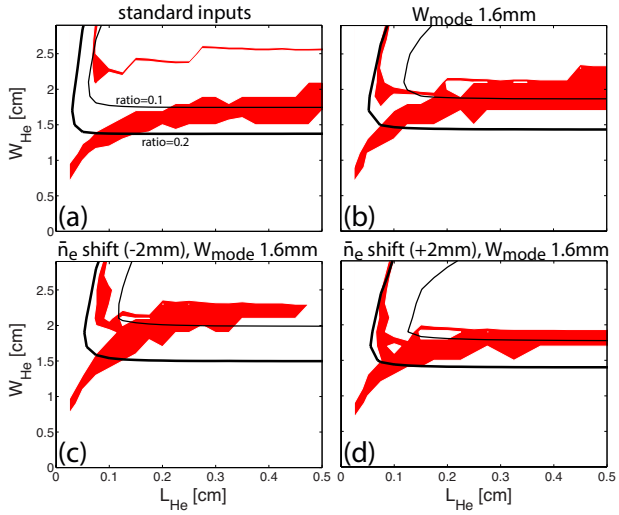

FIG. 13. Results from the synthetic diagnostic for different input mode widths (a-b) and different shifts between $\tilde{n}_e$ and $\bar{n}_e$ (c-d). Black curves are contours of constant ratio of the mode amplitude deduced from poloidal and toroidal optics (the 0.1 and 0.2 contours are shown). The red area indicates the region where the radial shift between poloidal and toroidal mode profiles is in the range between 1 mm and 1.6 mm.

An analysis similar to that in EDA H-mode is now performed for I-mode. There are some differences in the flux surface geometry near the LFS midplane between the two cases. The main differences in the input parameters for the synthetic diagnostic are, however, a longer poloidal wave length of the WCM ($k_{pol} = 1.6$ cm^{-1}) as compared to the QCM ($k_{pol} = 2$ cm^{-1}), a negligible radial shear of the mode, $\frac{\mathrm{d}\varphi}{\mathrm{d}r} \approx 0$, and the fact that I-mode does not have a density pedestal. The result of the synthetic diagnostic therefore depend only weakly on the relative shifts of $\tilde{n}_e$ and $\bar{n}_e$. In Fig. 14, we show the plots equivalent to those in Fig. 13 for the I-mode case. Fig. 14 (a) is obtained using the measured profiles as inputs, Fig. 14 (b) is obtained assuming a WCM profile substantially narrower than observed experimentally ($W_{mode} = 1.4$ mm instead of $W_{mode} = 2.4$ mm). The red areas indicate the regions consistent with the experimentally measured mode shift (0.9 ± 0.3 mm). The experimental mode amplitude ratio ($\approx 0.1 - 0.4$) is reproduced in the region to the top right of the black contour line.

We distinguish again two regions for which the synthetic diagnostic is consistent with the experiment. The region $L_{He} \geq 0.1$ cm, 1.5 cm $\leq W_{He} \leq 2$ cm and the region $L_{He} \approx 0.1$ cm, $W_{He} \geq 2$ cm. In the first region, the poloidal mode profile is shifted by $\lesssim 1$ mm. In the second region, similar to the H-mode case, inward shifts of the mode up to several mm are observed. At the same time, however, the simulated mode width is ≥ 4 mm, again substantially larger than in the experiments. Using a smaller input value for W_{mode} in Fig. 14 (b), the simulated mode width also decreases. For $L_{He} = 0.1$ cm, $W_{He} = 1.9$ cm, the simulated mode width is 3 mm and its peak location is shifted in by 1.8 mm. For $L_{He} = 0.125$ cm, $W_{He} = 2.3$ cm, the mode has a width of 3.4 mm and is shifted in by 2.2 mm. For the larger values of W_{He} in Fig. 14 (b) consistent with the experiment, the mode width increases further.

As in the case of H-mode, we find that amplitude ratios and shifts of the mode profiles from poloidal and toroidal optics can be reproduced without substantial absolute errors in the measured mode location. For $L_{He} \geq 0.1$ cm and 1.5 cm $\leq W_{He} \leq 2$ cm, this error is of the order of 1 mm or smaller. Larger shifts of ≈ 2 mm can, however, not entirely be excluded and are further discussed in the following section.

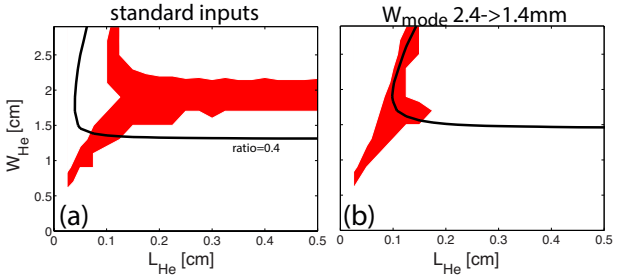

FIG. 14. The equivalent to Fig. 13 for I-mode. The red area indicates the region where the radial shift between poloidal and toroidal mode profiles is in the range between 0.6 mm and 1.2 mm.

C. Relative shifts between GPI and GP-CXRS measurements

To asses the role of instrumental effects for the relative alignment of mode profiles and E_r wells, we also need to consider possible instrumental effects for GP-CXRS. For this purpose, we have developed a synthetic diagnostic along the same lines as presented here for GPI[43]. This synthetic GP-CXRS diagnostic is combined with an iterative inversion algorithm to determine the "true" profiles, i.e., the profiles of impurity density, temperature, and flow, which, after application of the synthetic diagnostic, agree with the experimentally measured profiles. This procedure showed weak instrumental effects in EDA H-mode and I-mode plasmas. Motivated

by deuterium gas puff modeling in[29], a gas puff with a decay length of $L_D = 0.35$ cm and a width of $W_D = 2$ cm was assumed. In particular, instrumental effects were found not to sizably change the profiles of T_z and E_r or their relative position[34,43]. The situation is a bit more complicated here, as GP-CXRS measurements using helium gas puffs with a potentially shorter decay length are involved. Indeed, to radially align measurements from the discharge with a deuterium puff and a helium puff, respectively, we have forced profiles of T_z and V_{pol} from the two discharges to align, Fig. 4 (b), (d) and Fig. 5 (b), (d). We now investigate if this approach is justified for low values of L_{He}.

Figs. 15 (a) and (c) show profiles of T_z and V_{pol}, respectively, for the EDA H-mode case. Dashed blue profiles represent fits to the measurements obtained with GP-CXRS during the deuterium gas puff. The solid black curves are the inverted profiles obtained assuming a deuterium gas puff with $L_D = 0.35$ cm and $W_D = 2$ cm. Besides a relatively weak smoothing of the negative velocity peak, measured and inverted profiles are very similar. Applying now the synthetic diagnostic to the inverted profiles, assuming a helium gas puff with $L_{He} = 0.1$ cm and $W_{He} = 1.5$ cm, results in the dotted red profiles. We can see that these profiles differ slightly from those modeled for a deuterium puff, primarily by an inward shift of approximately 0.7 mm. This means that by forcing the profiles of T_z and V_{pol} obtained during the deuterium puff to align with those from the helium puff, Fig. 4 (b), (d), we introduced an artificial inward shift of the profiles from the deuterium puff discharge. In particular the E_r profile, therefore, appears shifted in relative to the QCM profile (which determined during the helium puff). For the parameters assumed here, this shift is 0.7 mm.

The net result of instrumental effects on the relative alignment of GPI and GP-CXRS measurements, assuming still a helium gas puff with $L_{He} = 0.1$ cm and $W_{He} = 1.5$ cm, is summarized in the first row of Table 1. The QCM profile determined with GPI from poloidal optics appears shifted out by 0.2 mm in this case. At the same time, instrumental effects of GP-CXRS and the alignment of data from the D_2 and He puff discharges result in an inward shift of the E_r well by 0.7 mm. The net effect, displayed in the last column of Table 1, is therefore that the QCM mode profile appears shifted out by 0.9 mm relative to the E_r well. If we assume instead a larger value for L_{He}, we find similar net shifts, row 2 and 3 in Table 1. In Sec. IV B, we have seen that gas puffs with a larger width and a smaller decay length also reproduce the experimental observations, except for the mode width at least. For these cases, we find that shifts of the mode and the E_r well partly cancel, row 4 of Table 1. Overall, these tests of instrumental effects suggest that the experimentally determined location of the poloidal QCM profile relative to the E_r well is not off by more than ≈ 1 mm.

The equivalent analysis is repeated now for I-mode and the result for a helium gas puff with $L_{He} = 0.1$ cm and $W_{He} = 1.5$ cm is plotted in Fig. 15 (b) and (d). It should be noted that in this case, the profiles measured during the D_2 puff could not be inverted for a gas puff with $L_D = 0.35$ cm and $W_D = 2$ cm and a smaller width of $W_D = 1$ cm was therefore assumed for the inversion. The results in Fig. 15 for I-mode are similar to those obtained for H-mode. The shorter decay length assumed here for the helium puff results again in an inward shift of the measured profiles. In the present case, this shift is about 0.9 mm. A summary of the results for different gas puff parameters consistent with the constraints in Fig. 14 is given in Table 1. This shows that the modeled shifts introduced by GP-CXRS mostly compensate those introduced by GPI, resulting in net shifts between mode profiles and E_r wells of $\leq$ 1mm.

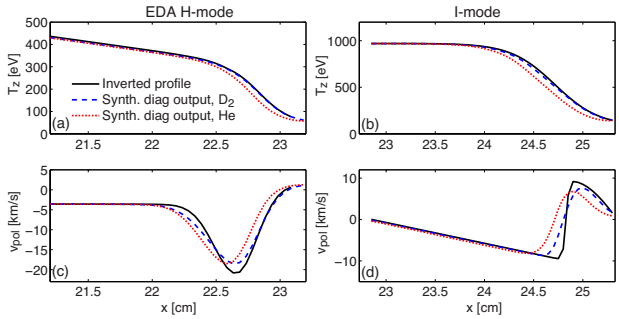

FIG. 15. Results from the synthetic GP-CXRS diagnostic for H-mode (left) and I-mode (right). Black profiles represent the inverted profiles, obtained by assuming a D_2 gas puff with $L_D = 0.35$ cm and $W_D = 2$ cm (H-mode) and $L_D = 0.35$ cm and $W_D = 1$ cm (I-mode). Dashed blue profiles represent the output of the synthetic diagnostic applied to the inverted profiles for the above gas puff parameters (these profiles match the measured profiles obtained during D_2 gas puffs). The dotted red profiles represent the output of the synthetic diagnostic applied to the inverted profiles assuming $L_{He} = 0.1$ cm and $W_{He} = 1.5$ cm.

V. SUMMARY AND CONCLUSIONS

Dedicated experiments have been performed to explore the radial location of quasi-coherent edge fluctuations in Alcator C-Mod pedestals. The focus here was on the QCM in EDA H-mode and the WCM and the GAM in I-mode plasmas. To probe these high power pedestals, optical diagnostics were used, primarily GPI for fluctuation measurements and GP-CXRS to obtain pedestal profiles of E_r, n_z, T_z, $V_{z,\theta}$, and $V_{z,\phi}$. To avoid uncertainties associated with measurements at different locations and through different optics, the same optics were used for GPI and GP-CXRS. For one discharge, a deuterium puff was used to obtain complete measurements from GP-CXRS, including the radial electric field profile. In a second discharge, the poloidal and toroidal

EDA H-mode

L_{He}	W_{He}	GPI shift	GP-CXRS shift	relative shift
[cm]	[cm]	[mm]	[mm]	[mm]
0.1	1.5	0.2	-0.7	0.9
0.2	1.5	0.6	-0.2	0.8
0.4	1.7	1.2	0	1.2
0.075	1.9	-1.8*	-1.1	-0.7

I-mode

L_{He}	W_{He}	GPI shift	GP-CXRS shift	relative shift
[cm]	[cm]	[mm]	[mm]	[mm]
0.1	1.5	-0.8	-0.9	0.1
0.2	1.5	-0.4	-0.2	-0.2
0.4	1.9	0.2	-0.1	0.3
0.1	1.9	-1.8*	-1.1	-0.7
0.125	2.3	-2.2*	-1.5	-0.7

TABLE I. Modeled profile shifts in H- and I-mode due to instrumental effects for different values of L_{He} and W_{He} consistent with the constraints in Figs. 13 and 14. Column 3 shows the shifts of the poloidal mode profiles obtained with the synthetic GPI diagnostic in Sec. IV B. Values with an asterisk correspond to the cases where a mode profile with reduced width was assumed. Column 4 shows the shift of E_r expected from instrumental effects as discussed in Sec. IV C. Column 5 shows the net relative shift of mode profile and E_r well. Positive values mean that the net effect is an apparent outward shift of the mode profile with respect to E_r.

GP-CXRS views in the mode region were connected to the GPI detectors and a helium gas puff was used. From these measurements, the mode profiles were evaluated with time domain Fourier analysis. Complete impurity temperature and poloidal flow profiles obtained with GP-CXRS during both discharges allowed correcting for shot-to-shot shifts of the pedestal location.

These measurements indicate that the QCM is located near the E_r well minimum and propagates along the ion diamagnetic drift direction in the plasma frame after accounting for the $E \times B$ drift. The WCM and GAM in I-mode are found here to be localized in the outer shear layer of the E_r well. The result is a relatively weak plasma frame phase velocity of the WCM, along the electron diamagnetic drift direction across most of its profile.

In order to estimate the role of instrumental effects associated with the applied mode localization procedure, we have introduced and studied a simplified synthetic GPI diagnostic. It takes into account the finite width of the optical chords, their angle with respect to the flux surface tangent at the location of the gas puff, and the curvature of the flux surfaces. The helium gas puff is parameterized by a radial decay length L_{He} and a lateral width W_{He}. This synthetic diagnostic shows that most accurate measurements of the mode location would be obtained for large L_{He}, small W_{He}, and/or optical views which are perfectly tangential to the flux surfaces at the gas puff location. For a realistic geometry and for most of the values of L_{He} and W_{He} explored with this synthetic diagnostic, mode profiles determined from toroidal optics appear shifted in with respect to the profiles measured using poloidal optics, consistent with experimental observations. Also consistent with experiment, the amplitude ratio of poloidal and toroidal mode profiles is ≤ 1. For small values of L_{He}, $\lesssim 0.075$ cm, and large W_{He}, $\gtrsim 2$ cm, the simulated poloidal and toroidal mode profiles appear shifted in by several mm compared to the actual mode location. However, for $L_{He} \geq 0.075$ cm and $W_{He} \approx 1.5$ cm, for which simulated mode amplitude ratios and shifts reproduce the experimental values and the simulated poloidal mode width is also realistic, the mode location from poloidal optics is found to be accurate to within ≈ 1 mm. Taking into account instrumental effects related to GP-CXRS measurements, we find, both in EDA H-mode and I-mode, a similarly small uncertainty for the relative alignment of mode profile and E_r well.

It is important to stress that previous probe measurements[10] in ohmic EDA H-mode imply a different result than found here. In this study, fluctuations across the QCM layer were detected by Langmuir probes and the local radial electric field and electron diamagnetic velocity were deduced from measurements of electron temperature, density and plasma potential profiles using the same Langmuir probes. These measurements found the QCM to be located in a region that spans the last-closed flux surface where E_r is near zero or slightly positive. The mode was found to propagate approximately at the electron diamagnetic drift velocity in the plasma frame. In order to obtain a qualitatively similar picture in the ion cyclotron range heated EDA H-mode plasmas presented here, the QCM would need to be approximately 3 mm further out with respect to the E_r well inferred from GP-CXRS, which exceeds the uncertainty deduced from the synthetic diagnostic study.

At this time, it is not understood why there exists a qualitative and quantitative difference between the deduced QCM properties in the two experiments. It may be related to the different levels of input power or it may indicate a systematic error in the interpretation of the data from one or both of these diagnostics. Resolving this is important, not only to unambiguously identify the nature of the QCM but also to provide a cross-check on the different diagnostic techniques. This study clearly highlights the need for several, redundant measurements to get complete, quantitative information on pedestal profiles and fluctuations. An important next step to improve the synthetic GPI diagnostic introduced here would be to constrain the assumed gas puff shapes by detailed helium gas puff modelling for C-Mod pedestal parameters.

ACKNOWLEDGMENTS

We would like to thank the entire Alcator C-Mod team for making these experiments possible and acknowledge support by US DOE Coop. Agreement No DE-FC02-99ER54512. This work has been carried out within the framework of the EUROfusion Consortium and has received funding from the Euratom research and training programme 2014-2018 under grant agreement No 633053. The views and opinions expressed herein do not necessarily reflect those of the European Commission. Support from the EUROfusion Researcher Fellowship programme under grant number WP14-FRF-EPFL/Theiler is acknowledged.

[1] A. Loarte, B. Lipschultz, A. S. Kukushkin, G. F. Matthews, P. C. Stangeby, N. Asakura, G. F. Counsell, G. Federici, A. Kallenbach, K. Krieger, *et al.*, Nucl. Fusion **47**, S203 (2007).

[2] T. E. Evans, R. A. Moyer, K. H. Burrell, M. E. Fenstermacher, I. Joseph, A. W. Leonard, T. H. Osborne, G. D. Porter, M. J. Schaffer, P. B. Snyder, P. R. Thomas, J. G. Watkins, and W. P. West, Nat. Phys. **2**, 419–423 (2006).

[3] P. T. Lang, A. Loarte, G. Saibene, L. R. Baylor, M. Becoulet, M. Cavinato, S. Clement-Lorenzo, E. Daly, T. E. Evans, M. E. Fenstermacher, Y. Gribov, L. D. Horton, C. Lowry, Y. Martin, O. Neubauer, N. Oyama, M. J. Schaffer, D. Stork, W. Suttrop, P. Thomas, M. Tran, H. R. Wilson, A. Kavin, and O. Schmitz, Nucl. Fusion **53**, 043004 (2013).

[4] K. H. Burrell, A. M. Garofalo, W. M. Solomon, M. E. Fenstermacher, D. M. Orlov, T. H. Osborne, J.-K. Park, and P. B. Snyder, Nucl. Fusion **53**, 073038 (2013).

[5] M. Greenwald, R. Boivin, P. Bonoli, R. Budny, C. Fiore, J. Goetz, R. Granetz, A. Hubbard, I. Hutchinson, J. Irby, B. Labombard, Y. Lin, B. Lipschultz, E. Marmar, A. Mazurenko, D. Mossessian, T. Sunn Pedersen, C. S. Pitcher, M. Porkolab, J. Rice, W. Rowan, J. Snipes, G. Schilling, Y. Takase, J. Terry, S. Wolfe, J. Weaver, B. Welch, and S. Wukitch, Phys. Plasmas **6**, 1943–1949 (1999).

[6] D. G. Whyte, A. E. Hubbard, J. W. Hughes, B. Lipschultz, J. E. Rice, E. S. Marmar, M. Greenwald, I. Cziegler, A. Dominguez, T. Golfinopoulos, N. Howard, L. Lin, R. M. McDermott, M. Porkolab, M. L. Reinke, J. Terry, N. Tsujii, S. Wolfe, S. Wukitch, Y. Lin, and Alcator C-Mod Team, Nucl. Fusion **50**, 105005 (2010).

[7] J. W. Hughes, P. B. Snyder, J. R. Walk, E. M. Davis, A. Diallo, B. LaBombard, S. G. Baek, R. M. Churchill, M. Greenwald, R. J. Groebner, A. E. Hubbard, B. Lipschultz, E. S. Marmar, T. Osborne, M. L. Reinke, J. E. Rice, C. Theiler, J. Terry, A. E. White, D. G. Whyte, S. Wolfe, and X. Q. Xu, Nucl. Fusion **53**, 043016 (2013).

[8] J. R. Walk, J. W. Hughes, A. E. Hubbard, J. L. Terry, D. G. Whyte, A. E. White, S. G. Baek, M. L. Reinke, C. Theiler, R. M. Churchill, J. E. Rice, P. B. Snyder, T. Osborne, A. Dominguez, and I. Cziegler, Phys. Plasmas **21**, 056103 (2014).

[9] J. W. Hughes, A. E. Hubbard, D. A. Mossessian, B. LaBombard, T. M. Biewer, R. S. Granetz, M. Greenwald, I. H. Hutchinson, J. H. Irby, Y. Lin, E. S. Marmar, M. Porkolab, J. E. Rice, J. A. Snipes, J. L. Terry, S. Wolfe, and K. Zhurovich, Fusion Sci. Technol. **51**, 317 (2007).

[10] B. LaBombard, T. Golfinopoulos, J. L. Terry, D. Brunner, E. Davis, M. Greenwald, and J. W. Hughes, Phys. Plasmas **21**, 056108 (2014).

[11] I. H. Hutchinson, R. Boivin, F. Bombarda, P. Bonoli, S. Fairfax, C. Fiore, J. Goetz, S. Golovato, R. Granetz, M. Greenwald, S. Horne, A. Hubbard, J. Irby, B. Labombard, B. Lipschultz, and et al., Phys. Plasmas **1**, 1511–1518 (1994).

[12] E. S. Marmar, S. G. Baek, H. Barnard, P. Bonoli, D. Brunner, J. Candy, J. Canik, R. M. Churchill, I. Cziegler, G. Dekow, L. Delgado-Aparicio, A. Diallo, E. Edlund, P. Ennever, I. Faust, C. Fiore, C. Gao, T. Golfinopoulos, M. Greenwald, Z. S. Hartwig, C. Holland, A. E. Hubbard, J. W. Hughes, I. H. Hutchinson, J. Irby, B. LaBombard, Y. Lin, B. Lipschultz, A. Loarte, R. Mumgaard, R. R. Parker, M. Porkolab, M. L. Reinke, J. E. Rice, S. Scott, S. Shiraiwa, P. Snyder, B. Sorbom, D. Terry, J. L. Terry, C. Theiler, R. Vieira, J. R. Walk, G. M. Wallace, A. White, D. Whyte, S. M. Wolfe, G. M. Wright, J. Wright, S. J. Wukitch, and P. Xu, Nucl. Fusion **55**, 104020 (2015).

[13] M. Greenwald, A. Bader, S. Baek, M. Bakhtiari, H. Barnard, W. Beck, W. Bergerson, I. Bespamyatnov, P. Bonoli, D. Brower, *et al.*, Phys. Plasmas **21**, 110501 (2014).

[14] M. Greenwald, N. Basse, P. Bonoli, R. Bravenec, E. Edlund, D. Ernst, C. Fiore, R. Granetz, A. Hubbard, J. Hughes, I. Hutchinson, J. Irby, B. LaBombard, Y. Lin, B. Lipschultz, E. Marmar, D. Mikkelsen, D. Mossessian, P. Phillips, M. Porkolab, J. Rice, W. Rowan, S. Scott, J. Snipes, J. Terry, S. Wolfe, and K. Zhurovich, Fusion Sci. Technol. **51**, 266 (2007).

[15] T. Golfinopoulos, B. LaBombard, R. R. Parker, W. Burke, E. Davis, R. Granetz, M. Greenwald, J. Irby, R. Leccacorvi, E. Marmar, W. Parkin, M. Porkolab, J. Terry, R. Vieira, and S. Wolfe, Phys. Plasmas **21**, 056111 (2014).

[16] R. M. McDermott, B. Lipschultz, J. W. Hughes, P. J. Catto, A. E. Hubbard, I. H. Hutchinson, R. S. Granetz, M. Greenwald, B. Labombard, K. Marr, M. L. Reinke, J. E. Rice, D. Whyte, and Alcator C-Mod Team, Phys. Plasmas **16**, 056103 (2009).

[17] A. E. Hubbard, D. G. Whyte, R. M. Churchill, I. Cziegler, A. Dominguez, T. Golfinopoulos, J. W. Hughes, J. E. Rice, I. Bespamyatnov, M. J. Greenwald, N. Howard, B. Lipschultz, E. S. Marmar, M. L. Reinke, W. L. Rowan, and J. L. Terry, Phys. Plasmas **18**, 056115 (2011).

[18] A. E. Hubbard, D. G. Whyte, R. M. Churchill, A. Dominguez, J. W. Hughes, Y. Ma, E. S. Marmar, Y. Lin, M. L. Reinke, and A. E. White, Nucl. Fusion **52**, 114009 (2012).

[19] A. E. Hubbard, T. Osborne, F. Ryter, *et al.*, Nucl. Fusion, submitted (2016).

[20] A. Dominguez, Ph.D. thesis, Massachusetts Institute of Technology, see http://dspace.mit.edu/handle/1721.1/79261 (2012).

[21] A. E. White, P. Phillips, D. G. Whyte, A. E. Hubbard, C. Sung, J. W. Hughes, A. Dominguez, J. Terry, and I. Cziegler, Nucl. Fusion **51**, 113005 (2011).

[22] I. Cziegler, P. H. Diamond, N. Fedorczak, P. Manz, G. R. Tynan, M. Xu, R. M. Churchill, A. E. Hubbard, B. Lipschultz, J. M. Sierchio, J. L. Terry, and C. Theiler, Phys. Plasmas **20**, 055904 (2013).

[23] X. Q. Xu, T. Y. Xia, N. Yan, Z. X. Liu, D. F. Kong, A. Diallo, R. J. Groebner, A. E. Hubbard, and J. W. Hughes, Phys. Plasmas **23**, 055901 (2016).

[24] J. L. Terry, R. Maqueda, C. S. Pitcher, S. J. Zweben, B. LaBombard, E. S. Marmar, A. Y. Pigarov, and G. Wurden, J. Nucl. Mater. **290**, 757–762 (2001).

[25] R. J. Maqueda, G. A. Wurden, S. Zweben, L. Roquemore, H. Kugel, D. Johnson, S. Kaye, S. Sabbagh, and R. Maingi, Rev. Sci. Instrum. **72**, 931–934 (2001).

[26] S. J. Zweben, D. P. Stotler, J. L. Terry, B. LaBombard, M. Greenwald, M. Muterspaugh, C. S. Pitcher, K. Hallatschek, R. J. Maqueda, B. Rogers, J. L. Lowrance, V. J. Mastrocola, and G. F. Renda, Phys. Plasmas **9**, 1981–1989 (2002).

[27] S. J. Zweben, D. P. Stotler, R. E. Bell, W. M. Davis, S. M. Kaye, B. P. LeBlanc, R. J. Maqueda, E. T. Meier, T. Munsat, Y. Ren, S. A. Sabbagh, Y. Sechrest, D. R. Smith, and V. Soukhanovskii, Plasma Phys. Control. Fusion **56**, 095010 (2014).

[28] I. Cziegler, J. L. Terry, J. W. Hughes, and B. LaBombard, Phys. Plasmas **17**, 056120 (2010).

[29] R. M. Churchill, C. Theiler, B. Lipschultz, R. Dux, T. Pütterich, E. Viezzer, and the Alcator C-Mod and ASDEX Upgrade Teams, Rev. Sci. Instrum. **84**, 093505 (2013).

[30] R. M. Churchill, B. Lipschultz, C. Theiler, and the Alcator C-Mod Team, Nucl. Fusion **53**, 122002 (2013).

[31]R. J. Fonck, D. S. Darrow, and K. P. Jaehnig, Phys. Rev. A **29**, 3288–3309 (1984).
[32]R. C. Isler, Plasma Phys. Control. Fusion **36**, 171–208 (1994).
[33]R. E. Bell, R. Andre, S. M. Kaye, R. A. Kolesnikov, B. P. Leblanc, G. Rewoldt, W. X. Wang, and S. A. Sabbagh, Phys. Plasmas **17**, 082507 (2010).
[34]C. Theiler, R. M. Churchill, B. Lipschultz, M. Landreman, D. R. Ernst, J. W. Hughes, P. J. Catto, F. I. Parra, I. H. Hutchinson, M. L. Reinke, A. E. Hubbard, E. S. Marmar, J. T. Terry, J. R. Walk, and the Alcator C-Mod Team, Nucl. Fusion **54**, 083017 (2014).
[35]A. Krämer-Flecken, S. Soldatov, H. R. Koslowski, and O. Zimmermann, Phys. Rev. Lett. **97**, 045006 (2006).
[36]L. Lao, H. St John, R. Stambaugh, A. Kellman, and W. Pfeiffer, Nucl. Fusion **25**, 1611 (1985).
[37]B. Cao, D. P. Stotler, S. J. Zweben, M. Bell, A. Diallo, and B. Leblanc, Fusion Sci. Technol. **64**, 29 (2013).
[38]P. Manz, P. Lauber, V. E. Nikolaeva, T. Happel, F. Ryter, G. Birkenmeier, A. Bogomolov, G. D. Conway, M. E. Manso, M. Maraschek, D. Prisiazhniuk, and E. Viezzer, Nucl. Fusion **55**, 083004 (2015).
[39]J. W. Hughes, D. Mossessian, K. Zhurovich, M. DeMaria, K. Jensen, and A. Hubbard, Rev. Sci. Instrum. **74**, 1667–1670 (2003).
[40]R. M. Churchill, C. Theiler, B. Lipschultz, I. H. Hutchinson, M. L. Reinke, D. Whyte, J. W. Hughes, P. Catto, M. Landreman, D. Ernst, C. S. Chang, R. Hager, A. Hubbard, P. Ennever, and J. R. Walk, Phys. Plasmas **22**, 056104 (2015).
[41]D. P. Stotler, B. LaBombard, J. L. Terry, and S. J. Zweben, J. Nucl. Mater. **313-316**, 1066–1070 (2003).
[42]R. J. Groebner, D. R. Baker, K. H. Burrell, T. N. Carlstrom, J. R. Ferron, P. Gohil, L. L. Lao, T. H. Osborne, D. M. Thomas, W. P. West, J. A. Boedo, R. A. Moyer, G. R. McKee, R. D. Deranian, E. J. Doyle, C. L. Rettig, T. L. Rhodes, and J. C. Rost, Nucl. Fusion **41**, 1789–1802 (2001).
[43]C. Theiler, R. M. Churchill, and B. Lipschultz, "Spatial resolution of the edge CXRS system on C-Mod," Alcator C-Mod Seminar (2013).